# Evaporation and Rheology Chart the Processability Map for Centrifugal Force Spinning

Peer-reviewed author version

MERCHIERS, Jorgo; Narvaez, Carina D. V. Martinez; Slykas, Cheryl; REDDY, Naveen & Sharma, Vivek (2021) Evaporation and Rheology Chart the Processability Map for Centrifugal Force Spinning. In: MACROMOLECULES, 54 (23) , p. 11061 -11073.

DOI: 10.1021/acs.macromol.1c01799
Handle: http://hdl.handle.net/1942/36869

**Evaporation and Rheology Chart the Processability Map for Centrifugal Force Spinning**

Jorgo Merchiers[1,2,†], Carina D. V. Martínez Narváez[3, †], Cheryl Slykas[3], Naveen K. Reddy[1,2]*, and Vivek Sharma[3*]

[1] Hasselt University, Institute for Materials Research (IMO-IMOMEC), B-3590 Diepenbeek, Belgium

[2] IMEC vzw–Division IMOMEC, Wetenschapspark 1, B-3590 Diepenbeek, Belgium

[3] Department of Chemical Engineering, University of Illinois at Chicago, Chicago, IL. 60608

[†]Equal contribution

Address correspondence to: viveks@uic.edu or naveen.reddy@uhasselt.be

Keywords: centrifugal spinning, spinnability, rheology, entangled polymers, rotary jet spinning, non-wovens

**Abstract**

We show that poly(ethylene oxide) (PEO) solutions formulated using solvent mixtures of acetonitrile (AcN) and water can be centrifugally-spun into fibers. We find that spinnability and fiber morphology depend on solvent choice if polymer concentration, solution shear rheology, the number of entanglements, extensional relaxation time, and the parameters for centrifugal spinning are nearly matched. We obtain an intrinsic spinnability map by contrasting the measured shear relaxation time with the evaporation rate determined using thermogravimetric analysis (TGA). Finally, we chart a processability map for centrifugal spinning by plotting extensional relaxation time, measured using a closed-cell dripping-onto-substrate (DoS) rheometry, against the time-of-flight (from the nozzle to the collector) by scaling both the timescales with an evaporation time. The processability map incorporates the influence of centrifugal spinning speed, nozzle diameter, distance from the collector, ambient conditions, and solvent and polymer properties, establishing an imitable paradigm for distinguishing between spinnable and sprayable formulations.

## INTRODUCTION

Centrifugal force spinning (CFS) has fast emerged as a method for producing continuous fibers or filaments from polymer solutions and melts, often with additives that enhance the functionality of resulting nonwoven structures.[1-3] Cotton candy as a product highlights the ease, rate, flexibility, and allure of this fiber/nonwoven manufacturing process and its scalability. Many recent studies focus on centrifugal spinning polymer solutions[4-7] to take advantage of room temperature processing and the possibility of producing finer fibers without the need for superfine nozzles, melt-processable polymers, and methods like electrospinning that require high voltage sources and work with a limited range of solvents.[1, 4, 8, 9] However, a combination of complex free-surface flow and instabilities, non-Newtonian fluid properties that change due to evaporation or solidification, mass or heat transfer (often both), as well as polymer stretching, orientation and crystallization, accompany the formation of centrifugally spun fibers.[10-13] The coupling of multiple transport processes and non-Newtonian fluid mechanics present formidable challenges to creating a CFS processability map and connecting spinnability, heuristically identified with the ability to make fibers with the process and material parameters. Several theoretical and simulation studies probe the influence of non-Newtonian rheology and fluid mechanics in dictating the initiation, extension, and thinning of the spiraling jet from a fast-rotating spinneret or nozzle, the role of viscoelastic free surface flows and instabilities, and the influence of evaporation or solidification process.[10-14] The significant impact of process parameters like spinning speed, nozzle shape and size, distance to the collector and airflow, and varying polymer concentration and molecular weight on fiber diameter and morphology are tabulated and discussed in several experimental and theoretical studies.[1, 4-7, 10-18] However, fundamental questions remain about the impact of solvent choice, through influence on rheological response, especially to extensional flows and evaporation, in dictating spinnability, motivating this study.

Here, we highlight the influence of changing solvent properties on spinnability and final fiber morphology under matched processing conditions by formulating the spinning dopes as solutions of 3 wt.% and 5 wt.% PEO in acetonitrile (AcN) and water mixtures. Variation in AcN weight fraction influences the volatility, surface tension, density, viscosity, dielectric constant, and polymer-solvent interactions. Several centrifugal force spinning (CFS) (and likewise, electrospinning (ES)) studies have explored the influence of the solvent choice on the morphology of fibers formed by poly(ethylene terephthalate) (PET), poly(vinyl pyrrolidone) (PVP), and polylactide (PLA),[13, 18-20] and PEO fibers[21-23]. Still, the use of neither electrospinning nor CFS is described before for making fibers from PEO solutions formulated in AcN:$H_2O$ solvent mixtures. The choice of PEO solutions is motivated by three factors. Firstly, the formation, morphology, and properties of PEO fibers are the focus of many fundamental studies.[1, 3, 5, 10, 15, 24-37] Secondly, fibers formed by PEO alone, using PEO to enhance spinnability, or containing PEO blended with other polymers, particles, or proteins, are considered suitable for applications ranging from drug delivery, antimicrobial filters, battery separators, photovoltaics, and separation membranes.[24, 25, 30, 34-40] Thirdly, we have extensively characterized shear, and extensional rheology response of aqueous PEO solutions,[41-45] and recently showed, that PEO fiber mats centrifugally spun with entangled PEO solutions in pure AcN rival crystallinity and mechanical properties of electrospun PEO fibers.[46]

This contribution identifies and discusses the timescales for solvent loss and fiber formation, compared to several intrinsic timescales in the problem, to construct a processability map. The time-of-flight from the nozzle to the collector depends on the rotational rate, the distance between the collector and the spinneret, and the trajectory of the spiraling jet. It can be compared to (liquid) jet-fiber (solid) transformation time, $t_{jf}$. For solution-CFS, the molecular diffusion within the drying polymer solution jet and hydrodynamic processes that assist in solvent vapor removal from fiber surface set the evaporation-based time, $t_{jfe}$. In melt-CFS, the

phase transition kinetics due to cooling below crystallization and glass transition temperatures set solidification-based time, $t_{jfm}$, and in reactive-CFS, polymerization reaction kinetics determine the reaction-limited time, $t_{jfr}$.[15, 16] The spiraling liquid jet undergoes drawing and thinning primarily under the influence of stresses contributed by inertia, centrifugal forces, capillarity, viscoelasticity, and aerodynamic drag.[10-13, 18] The interplay of different stresses can drive or delay the formation and growth of a capillarity-driven instability that must be controlled and understood to obtain continuous fibers rather than drops. The challenges in quantifying nonlinear rheology, non-Newtonian fluid mechanics, and pinching dynamics that influence dispensing of rheologically complex fluids led Clasen *et al.*[47] to christen a potential processability map as "a map of misery". However, the fiber formation from polymer solutions additionally involves mass transfer considerations, though concentration-dependent and humidity-influenced phase behavior can also play a role. A review of theoretical models of CFS or ES (or any fiber spinning techniques),[9-14, 18, 48, 49] and the previous attempts at describing spinnability or stringiness,[9-15, 18, 48-52] presents us with a formidable array of parameters appearing in coupled, intricate transport equations, with additional nonlinearities introduced by viscoelasticity, free surfaces, and evaporation from mobile jets.

Here, we set ourselves the task of abstracting, charting, and presenting a pragmatic and easily computable processability map based on the timescales that can be measured experimentally and estimated theoretically in a straightforward manner. We characterized the shear rheology response using torsional rheometry and identified the unentangled and entangled regimes by examining the concentration-dependent variation in zero shear viscosity. We obtained a measure of shear relaxation time form the onset of shear thinning, and determined the extensional relaxation time using dripping-onto-substrate (DoS) rheometry.[41-44, 53, 54] The DoS rheometry setup, design considerations, specific advantages contrasted to other extensional rheology methods, and various approaches to analyzing datasets are detailed in our

previous contributions,[41-45, 53-61] and in several recent studies.[62-71] The measured extensional relaxation time, $\lambda_E$ usually differs in magnitude and concentration-dependent variation from the shear relaxation time due to the role played by stretched chain hydrodynamics.[41-45, 61, 72-83] The response to extensional deformations is relevant for fiber spinning as well as any jetting or spraying applications. We opted for closed-cell DoS rheometry to minimize evaporation, as volatile entangled polymers solutions exhibit strong concentration-dependent variation in rheology. We also measured the evaporative mass loss as a function of time using thermogravimetric analysis (TGA). Finally, we show that plotting shear relaxation time against TGA-based evaporation rate produces an intrinsic spinnability map with sufficient contrast for identification of spinnable regime using CFS with matched processing conditions. Finally, we outline a pragmatic processability map that incorporates the influence of processing conditions and extensional rheology effects by choosing extensional relaxation time and time-of-flight scaled with relative evaporation time as coordinates.

## MATERIALS AND METHODS

Poly(ethylene oxide) or PEO of molecular weight, $M_w$ = 600 kg/mol (Sigma-Aldrich) was dissolved in acetonitrile (AcN) solvent (HPLC grade, VWR chemicals) under mild mixing conditions, as long flexible chains are known to be prone to chain scission. The molecular weight of PEO was checked before and after mixing, and no differences were observed. We spun PEO fibers using a bespoke centrifugal force spinning (CFS) set-up designed at Hasselt University with the flexibility for changing nozzle type and material and with shifting and lifting mechanisms that allow control over nozzle-collector distance.[17, 46] The influence of nozzle properties and rotational speed on fiber formation and morphology are detailed in a previous contribution.[17] We centrifugally spun fibers for a range of PEO concentrations with matched processing parameters like rotational speed (4000 rpm), temperature (298 K), distance to the collector (12 cm), and nozzle diameter (0.6 mm). The SEM images were acquired using

a ZEISS Gemini 450 (Zeiss, Zaventem, Belgium). The fiber diameter and standard deviation were analyzed in ImageJ. Mass loss as a function of time for the polymer solutions as measured using thermogravimetric analysis (TGA) using Q50 apparatus (TA Instruments, New Castle, DE, USA) at a fixed temperature of 25°C and under a nitrogen atmosphere, with a flow rate of 90 mL/min. The steady shear viscosity was characterized using cone-and-plate geometry (50 mm diameter, 1° cone angle) on an Anton Paar MCR 302 Rheometer (torque range $10^{-5}$ - 200 mN-m), and we checked that the polymer solutions utilized on both sides of the Atlantic had similar shear rheology response. The steady shear viscosity, $\eta(\dot{\gamma}) \equiv \tau_{12} / \dot{\gamma}$ was calculated from the measured shear stress, $\tau_{12}$ from imposed shear rates in the range of $\dot{\gamma}$= 0.01-$10^3$ $s^{-1}$. The temperature was maintained using a Peltier element, and we used a solvent trap to minimize the influence of solvent evaporation on the measurements.

We characterized the extensional rheology response of the PEO solutions using dripping-onto-substrate (DoS) rheometry. A finite volume of fluid is dispensed through a stainless-steel nozzle and is deposited on a clean glass substrate at a height *H* below the nozzle. The nozzle radius is kept constant for all experiments for the PEO solutions with outer diameter, $2R_0 = 2.108\,\mathrm{mm}$ and an inner diameter of $D_i = 1.6\,\mathrm{mm}$. The fluid is pumped at a low and fixed flow rate ($Q$ = 0.02 mL/min) and an aspect ratio of $H/D_0 \approx 3$. The imaging system includes a light source, a diffuser, a high-speed camera (Fastcam SA3 with a Nikkor 3.1 x zoom (18-25 mm) lens), and an attached macro lens to improve magnification at the frame rates used (8000 – 25000 frames per second). We used a closed transparent cell to carry out experiments in an atmosphere saturated with solvent vapor. Even though we find that evaporation exercises negligible influence for unentangled aqueous solutions, a closed cell is needed for volatile, entangled (VE) polymer solutions that display strong concentration-dependent change in rheology. The DoS videos are analyzed with ImageJ and specially written MATLAB codes to determine the minimum neck radius as a function of time.

## RESULTS AND DISCUSSION

**Centrifugal force spinning of PEO fibers from AcN:$H_2O$ solutions:** A home-built centrifugal fiber spinning set-up, included in Figure 1a as a labeled photograph, was used to produce fibers from PEO solutions prepared in AcN:$H_2O$ solvent mixtures. The set-up consists of two symmetrically mounted nozzles and the possibility to move pillars or raise base provides an adjustable collector-nozzle distance, as detailed previously[17]. Figure 1b shows a snapshot highlighting the deposition process, whereas Figure 1c shows a fiber mat after collection. Fibers were centrifugally spun with matched processing parameters and similar environmental conditions. The rotational speed, collector distance, and nozzle diameter were set at fixed values of 4000 rpm, 12 cm, and 0.6 mm, respectively.

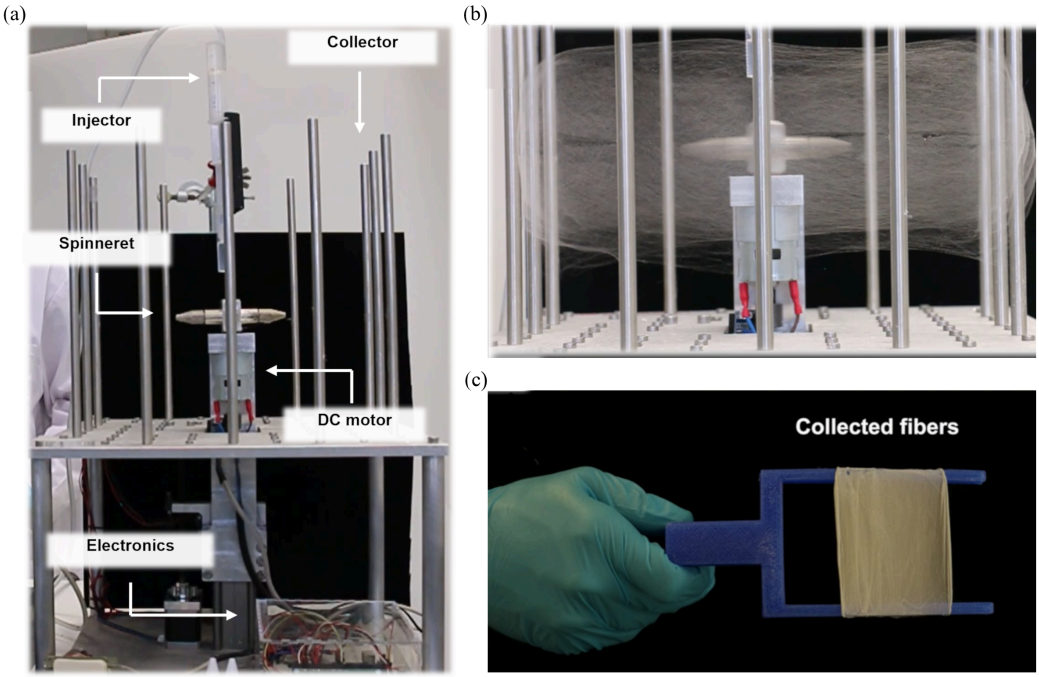


**Figure 1. Centrifugal force spinning apparatus used for prepared PEO fiber mats.** (a) Photograph of the home-built centrifugal force spinning or rotary jet spinning set-up. The labels mark the critical parts of the apparatus, including an injector, a spinneret, a DC motor, and the electronics that allow control over the rotational speed. b) A snapshot showing the fiber spinning process that deposits continuous fibers on the collectors. c) Image shows an example of a fiber mat formed with the collected fibers.

The centrifugal spinning of PEO solutions in pure acetonitrile produced a spray of droplets for $c < 2$ wt. %, beaded fibers for 2 - 3 wt. %, and continuous fibers for 4 - 6 wt. %.

Centrifugal forces generated by the chosen processing parameters produce insufficient stress to create continuous jets for polymer concentration beyond 6 wt.%. Thus, the spinnability range of PEO/AcN solutions for centrifugal fiber spinning at 4000 rpm lies between 2 and 6 wt. %. We spun PEO solutions in AcN:$H_2O$ solvent mixtures to evaluate solvent composition, which leads to a variation in material properties like surface tension, solvent viscosity, and vapor pressure, which impacts spinnability and fiber morphology. For this comparison, we used matched processing parameters like rotational speed (4000 rpm), temperature (298 K), distance to the collector (12 cm), and nozzle diameter (0.6 mm). Figure 2 shows SEM images of fibers obtained by centrifugal force spinning for $c = 3\ \mathrm{wt.\%}$ and $c = 5\ \mathrm{wt.\%}$ polymer solutions in four solvent mixtures as well as pure AcN as a solvent.

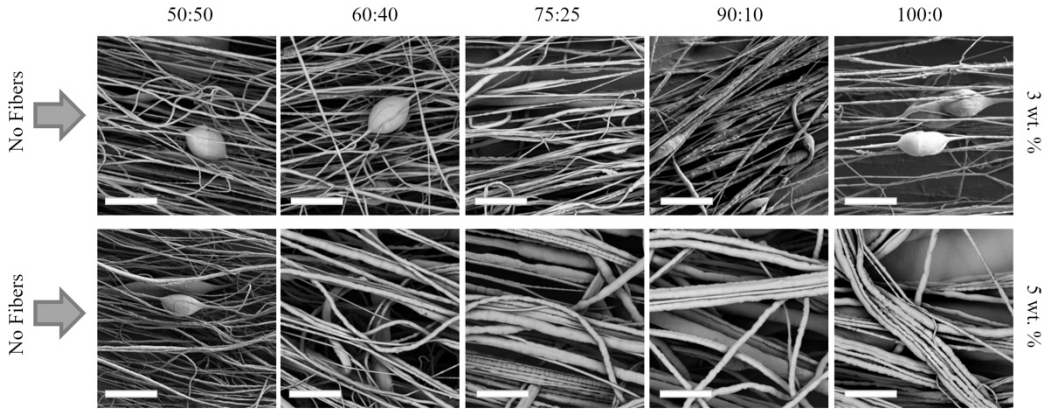


**Figure 2. SEM images of the centrifugally spun PEO fibers**. In each row, the concentration of AcN added to the solvent mixture increases from left to the right. In contrast, each column compares the influence of change in polymer concentration for the indicated mixed solvent. The scale bar is 20 microns.

Solutions prepared in pure water yielded only a spray of droplets, whereas in pure AcN, continuous fibers form. No fibers form if the AcN fraction is below 50% of the solvent, few beads on the fiber web appear if PEO with $c = 3\ \mathrm{wt.\%}$ in 50%, 60%, and pure AcN is centrifugally-spun. PEO solutions with 90:10 AcN:$H_2O$ have reduced the bead formation, whereas the 75:25 solvent mixture shows the complete disappearance of beads. The fiber diameters of the 90:10 and 75:25 solvent compositions are comparable, but the 60:40 and 50:50 AcN:$H_2O$ solvent mixtures show finer diameters. Solutions with 5 wt. % PEO show no fibers

for AcN fraction below 50%, a few beads for 50:50 AcN:$H_2O$, and continuous fibers for solvent mixture with AcN fraction equal to and above 60%. The fiber diameters appear comparable for the 90:10 and 75:25 solvent mixtures, and lower diameters appear for 60:40 and 50:50 AcN:$H_2O$. Assuming the differences are caused by rheology and evaporation effects, we made the measurements described next.

**Steady shear viscosity and relaxation time of PEO/AcN solutions:** Steady shear viscosity as a function of shear rate, $\dot{\gamma}$, is plotted in Figure 3a for 5 wt.% PEO solutions. The rate-dependent viscosity datasets, with a Newtonian plateau at low shear rate followed by shear thinning response, observed at all concentrations (see black solid lines in Figure3a), are captured using the Carreau model[84] expression:

$$\eta(\dot{\gamma}) = \eta_\infty + \frac{\eta_0 - \eta_\infty}{(1+(\dot{\gamma}/\dot{\gamma}_c)^2)^{\frac{n-1}{2}}} \qquad (1)$$

Here, $\eta_0$ and $\eta_\infty$ correspond to the rate-independent zero shear viscosity and the infinite shear rate viscosity, respectively. Defining $\eta_\infty$ as equal to the solvent mixture viscosity reduces the total number of free parameters to three. The exponent $n$ quantifies the power law dependence of the viscosity at intermediate shear rates and a critical shear rate, $\dot{\gamma}_c$, captures the onset of the power law region that allows the computation of the shear relaxation time, $\lambda_c = \dot{\gamma}_c^{-1}$. Zero-shear viscosity, $\eta_0$ values as a function of PEO concentration in pure water and pure acetonitrile solutions are shown in Figure 3b. Aqueous PEO solutions exhibit higher viscosity than PEO in acetonitrile solutions at matched concentrations. Three regimes identified for the aqueous PEO solutions show $\eta_0 \propto c^k$ with $k$ = 1, 2, and 4.4. The respective three powers correspond to the dilute, semi-dilute, unentangled and semi-dilute, entangled regimes.[85] Graphically, the entanglement concentration, $c_e \approx 1.8\,\mathrm{wt.\%}$ appears to be comparable in both solvents, implying that 3 wt.% and 5 wt.% PEO solutions used in this study lie in the entangled regime.

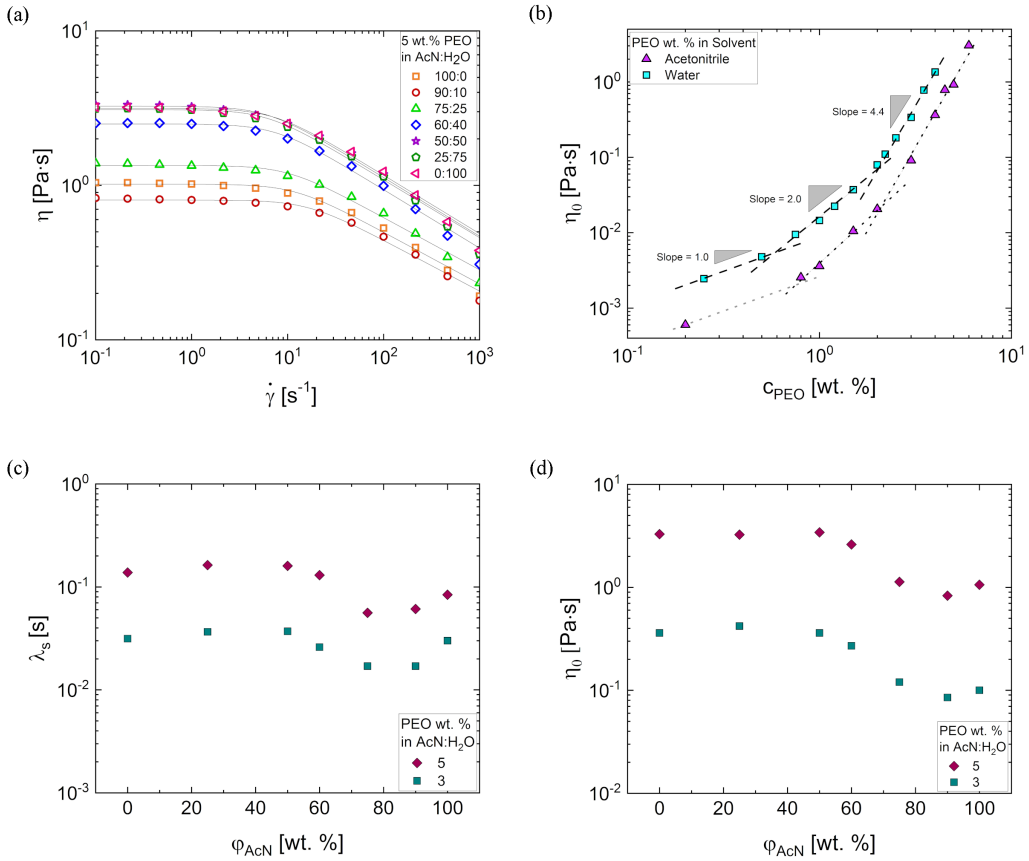


**Figure 3. Influence of AcN fraction on shear rheology response of PEO solutions.** (a) Steady shear viscosity as a function of shear rate for 5 wt.% PEO solutions displays an AcN weight fraction dependent variation and shear thinning response. The Carreau model fits are shown as solid black lines. (b) A concentration-dependent increase in zero shear viscosity as a function of PEO in pure water shows larger values than pure acetonitrile solutions at matched concentrations. (c) Shear relaxation time and (d) zero shear viscosity of 3 and 5 wt.% PEO solutions as a function of AcN fraction in solvent mixtures display a non-monotonic variation.

Figure 3c and Figure 3d respectively show apparent shear relaxation time, $\lambda_c = \dot{\gamma}_c^{-1}$ and zero shear viscosity values, extracted from the Carreau model fit to steady shear viscosity. Both $\eta_0$ and $\lambda_c$ exhibit a non-monotonic variation as a function of the AcN:$H_2O$ ratio with a dip at 75:25 and 90:10. Previous studies attribute a similar dip to the changes in polymer conformation due to the variation of hydrogen-bonding interactions and preferential adsorption/hydration of PEO as a function of the water content in the binary mixtures.[86] Entangled PEO solutions in acetonitrile appear to form continuous fibers. In contrast, the entangled aqueous PEO solutions form a jet that splashes off the collector even though the zero shear viscosity of aqueous solutions is higher. Even though many studies on spinnability (mainly in electrospinning

context) argue that spinnable solutions tend to form above entanglement concentration,[87-89] our observations show that solutions with similar state of overlap and entanglements, as well comparable shear viscosity, can display dramatically distinct spinnability and fiber morphology, implying that the role of extensional rheology and solidification process needs to be evaluated, as discussed in the next two sections.

**Extensional relaxation time of entangled PEO solutions:** The set-up for DoS rheometry is shown in the schematic included as Figure 4a. The DoS rheometry protocols rely on the visualization and analysis of capillarity-driven pinching dynamics of liquid necks, in analogy with other capillarity-based techniques, like CaBER (Capillary break-up extensional rheometer) and other stretched liquid bridges,[90-98] dripping,[73, 99, 100] or jetting-based rheometry.[101-106] Figure 4b shows the neck shapes and shape evolution for three AcN:$H_2O$ ratios. Three snapshots of the image sequence from the last stage before pinch-off exhibit the pronounced cylindrical filament shape. We contrast neck shapes observed at the same scaled radius at an early stage. Even though the shear viscosity of PEO solutions in pure water are higher than the pure AcN at matched concentrations, the overall filament lifespan appears to be longer in AcN added solutions, requiring the use of specific time intervals for each solvent. The radius evolution plots in Figure 4c initially display a viscocapillary (VC) response with a linear decrease in neck radius, followed by an elastocapillary (EC) regime that displays an exponentially slow decay in the radius. The EC regime results from an interplay of capillarity and nonlinear viscoelastic stresses that arise in response to extensional flows associated with streamwise velocity gradients in the pinching necks. The simplest EC expression by Entov and coworkers, that is rederived or discussed in studies based on the Oldroyd-B model[72, 101, 104, 107-112] uses the shear modulus, $G$ and shear relaxation time, $\lambda_s$ as parameters. It thus lacks due consideration of additional effects including non-Hookean elastic response, finite extensibility, and conformation-dependent drag that arise in response to strong flows for both unentangled

and entangled solutions.[42-44, 78-84, 90, 113] Therefore, we use the following modified expression (introduced by Dinic and Sharma[43])

$$\frac{R(t)}{R_0} = \left(\frac{G_E R_0}{2\sigma}\right)^{1/3} \exp\left(-\frac{t-t_c}{3\lambda_E}\right) \qquad (2)$$

as it accounts for the onset of EC at $t_c$, and computes an apparent extensional modulus, $G_E$ distinct from the corresponding shear values.[41-44, 53]

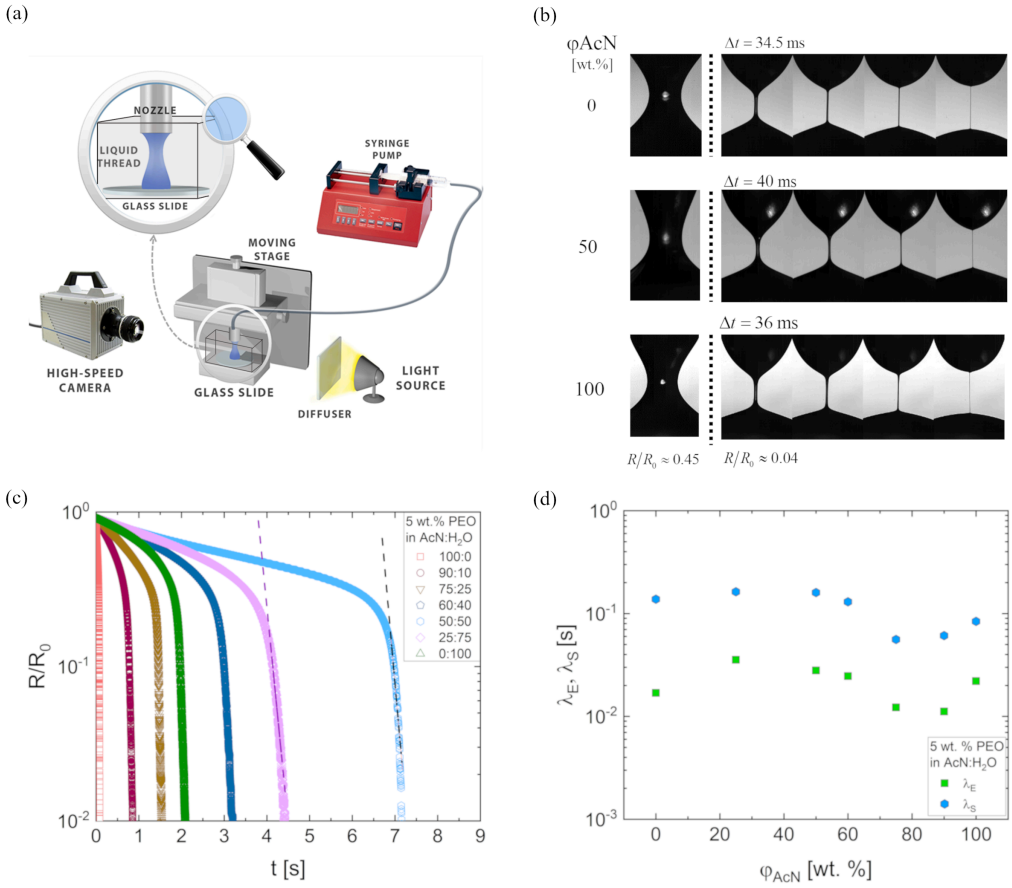


**Figure 4. Pinching dynamics and extensional relaxation times of PEO in AcN:$H_2O$ mixtures.** (a) Dripping-onto-Substrate (DoS) schematics include an imaging and dispensing system. DoS involves the visualization and analysis of an unstable liquid neck formed by a finite volume of fluid released onto a fixed substrate (zoomed-in image shows the closed cell). (b) Snapshots show neck shape evolution of 5 wt.% PEO in three AcN:$H_2O$ / water mixtures. The first column corresponds to the neck shape at a matched $R/R_0 = 0.45$. The last three columns with time steps of 34.5, 40, and 36 ms for 0, 50, and 100 AcN content, respectively, highlight the slender cylindrical filament characteristic of an EC response. (c) Radius evolution data acquired using dripping-onto-substrate (DoS) rheometry plotted on a semilog scale show a pronounced elastocapillary regime and AcN concentration-dependent variation in the filament lifespan. (d) Extensional relaxation time as a function of the AcN fraction shows a nonmonotonic behavior that mimics the variation observed for shear relaxation time.

The extensional relaxation time, $\lambda_E$ values measured for the 5 wt.% solutions, included in Figure 4d, correlate well with shear relaxation time, $\lambda_s$ and we find that chain dynamics and rheology are not influenced substantially by change in AcN concentration. Furthermore, the extensional relaxation time, $\lambda_E < \lambda_s$ for these entangled PEO solutions (both 3 and 5 wt.% solutions). The lower value of $\lambda_E$ for entangled solutions is attributed to the influence of disentanglement and high stretch of the chains, contributed by non-Hookean elasticity, finite extensibility, and conformation-dependent drag.[82, 114-121] In contrast, dilute polymer solutions display $\lambda_E > \lambda_s$ attributed to the dramatic change in conformation, particularly for highly flexible, highly extensible polymers like PEO that can undergo coil stretch-transition in response to extensional flow, leads to longer extensional relaxation time, for, as detailed elsewhere.[41, 43, 44, 72-75, 79, 80]

As the unique advantages of DoS rheometry lie in facilitating the characterization of low viscosity (<100 mPa.s) and low elasticity formulations (beyond the range of techniques), most of the published studies describe extensional relaxation time of unentangled polymer solutions.[41-44, 53-56, 60-63, 65, 67, 122] Even though a few DoS rheometry studies explore the extensional rheology of the entangled solutions of polysaccharides and polyelectrolytes,[44, 54-57] there are no previous DoS rheometry studies of the entangled solutions of uncharged polymers, explored herein for the PEO solutions. However, the CaBER measurements carried out with aqueous PEO solutions also display $\lambda_E < \lambda_s$ values, in agreement with Figure 4b. It is well-established that the knowledge of rate-dependent shear viscosity is not adequate to estimate or predict the strain and strain-rate dependent extensional viscosity (also referred to as tensile growth coefficient), $\eta_E = \eta_E^+(t, \dot{\varepsilon})$ of even solutions and melts of bare polymers, and shear thinning polymer solutions can exhibit pronounced extensional hardening.[41-44, 51, 53-56, 90, 123, 124] Our preliminary studies using dripping-onto-substrate (DoS) rheometry protocols reveal that these entangled solutions also display strain hardening in response to extensional flows. A more

detailed investigation of polymer concentration-dependent variation in shear and extensional rheology response for these PEO solutions in AcN:$H_2O$ is underway, and therefore, here we keep focus only on the estimation and comparison of the extensional relaxation time values, and relevance for assessing spinnability.

**Evaporation timescales of AcN:$H_2O$ solvent mixtures:** To contrast the differences in solvent loss over time in centrifugal spinning, we measured the mass loss from 30 mg of PEO solutions (with 5 wt. % polymer added) as a function of time using thermogravimetric analysis (TGA). The plots of mass loss as a function of time included in Figure 5a show that increasing the AcN fraction speeds up the solvent removal process. We can analyze the evaporation data using a simple mass transfer model that accounts for diffusion-limited mass transfer within the polymer solution and a boundary condition that incorporates the role of outside airflow using a mass transfer coefficient, as detailed in Sharma et al.[125, 126] While the model description becomes less realistic at later stages when the formation of polymer-rich shell impacts the diffusivity itself, the experimental datasets and plots include the effect of such a shell. Nevertheless, inspired by the simplified model, [125, 126] we fit the mass loss data with an exponential decay function and estimate an evaporation time, $t_{evTGA}$ from the decay constant. The $t_{evTGA}$ values obtained from TGA data are plotted in Figure 5b and include the influence of solvent diffusivity within the liquid layer and the mass transfer coefficient that itself depends on the flow velocity and material properties of the surrounding gas phase. Here we used a nitrogen atmosphere and flow rate of 90 mL/min. However, the measurement of solvent evaporation time using TGA involves no convective flow within the solution that can emulate flows that arise during fiber spinning and dispensing or coating processes. As the mass transfer coefficient depends on the sample geometry and ambient conditions (temperature, humidity, and gas velocity field), a suitable conversion factor is needed to determine mass loss during fiber spinning from TGA data. Additionally, during spinning, the rate of mass loss is influenced by changes in macromolecular

conformation (stretching) and orientation. Nevertheless, the evaporation timescale extracted from TGA measurements (Figure 5) characterizes the intrinsic differences in the evaporative loss of the solvent under matched conditions.

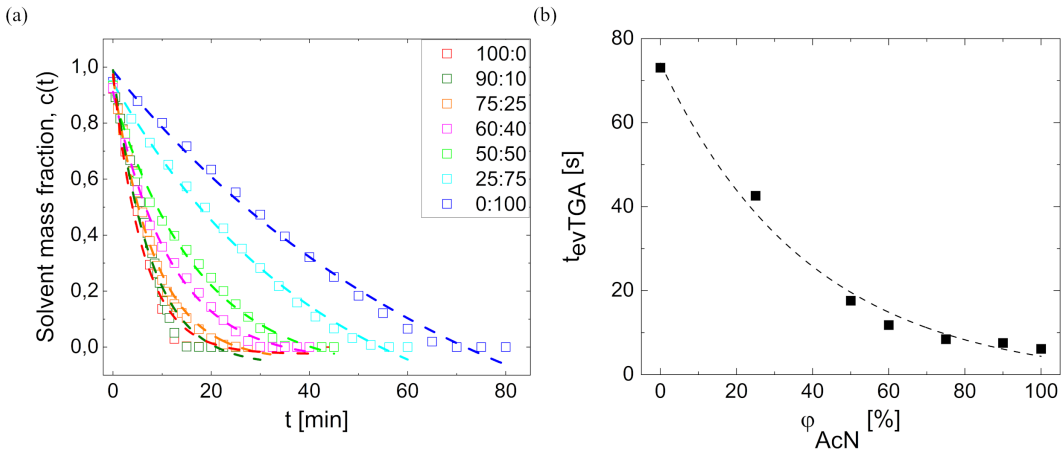


**Figure 5. Mass loss and evaporation time are influenced by solvent choice.** (a) Mass loss as a function of time (symbols) as measured using TGA (Q50 apparatus, TA Instruments, New Castle, DE, USA) at a fixed temperature of 25 °C and under a nitrogen atmosphere. The dotted line fits an exponential decay function of the form $c(t) = A \exp(-t/t_{evTGA})$ to the mass loss data for 5 wt. % PEO solutions in different solvent compositions. (b) Evaporation time computed using TGA data, illustrating how the addition of AcN significantly decreases the solidification time compared to aqueous solutions.

**Processability diagram based on the evaporation timescale, relaxation times, and time-of-flight:** The collection of fibers on the collector requires the formation of a stable spiraling jet that undergoes solidification before instability growth and before reaching the collector. The consideration leads to the identification of at least three crucial, relevant timescales: instability growth time, evaporation time, and time-of-flight. The growth of sinusoidal instability as well as pinching dynamics of necks of viscous fluids depends on the interplay of viscous stress and capillary pressure, with a characteristic time known as the viscocapillary time, $t_{vc} = \eta_0 D_0/\sigma$, and a dimensionless viscosity, expressed as Ohnesorge number, $Oh = \eta/\sqrt{\rho\sigma D_0}$ that equals to the ratio of viscocapillary time, $t_{vc}$ to inertiocapillary time, $t_{ic} = \sqrt{\rho R_0^3/\sigma}$.[90, 101, 104, 127] The intrinsic elastocapillary number, $Ec = \lambda_s\sigma/\eta_0 D_0 = \sigma/GD_0$ captures the influence of capillary stresses in comparison with elastic stresses on capillary-driven instability growth.[90, 128] Table 1

lists the values of these timescales and dimensionless groups obtained from the knowledge of shear rheology response, and includes timescales obtained using evaporation rate (TGA) and extensional rheology (DoS) measurements. The values listed in Table 1 show that shear viscosity changes by nearly a factor of three, surface tension changes by almost a factor of 2, and hence $t_{vc}$ values remain roughly unchanged as the AcN fraction is varied. But as the relaxation time values change by no more than a factor of 2, the values of Ec also remain roughly unchanged as the AcN fraction is varied. Table 1 shows that only evaporation rate shows a considerable variation as a function of the AcN fraction.

**Table 1: Influence of solvent composition on rheology and evaporation**

| AcN fraction | $\eta_0$ [Pa·s] | $\lambda_s$ [s] | $\lambda_E$ [s] | $t_{VC}$ [s] | Ec | $t_{evTGA}$ [s] | $\frac{t_{evTGA}}{t_{evTGA,100}}$ | $De_s$ |
|---|---|---|---|---|---|---|---|---|
| 100 | 1.06 | 0.084 | 0.022 | 0.018 | 4.6 | 6.15 | 1 | 0.0137 |
| 90 | 0.83 | 0.061 | 0.0112 | 0.014 | 4.3 | 7.55 | 1.23 | 0.0081 |
| 75 | 1.13 | 0.056 | 0.0122 | 0.019 | 2.9 | 8.42 | 1.37 | 0.0067 |
| 60 | 2.61 | 0.011 | 0.0247 | 0.045 | 2.9 | 11.8 | 1.92 | 0.0110 |
| 50 | 3.42 | 0.16 | 0.0280 | 0.059 | 2.8 | 17.6 | 2.86 | 0.0091 |
| 25 | 3.25 | 0.16 | 0.0355 | 0.049 | 3.3 | 42.6 | 6.93 | 0.0038 |
| 0 | 3.29 | 0.14 | 0.0169 | 0.028 | 4.9 | 73.1 | 11.9 | 0.0019 |

Several researchers have outlined processability maps by contrasting different timescales, length scales or forces in the problem. Ren et al.[13] constructed an "operating diagram" using a plot of $Oh$ against a Weissenberg number, $Wi = \lambda_s \dot{\gamma}$ (compares relaxation time to the timescale equal to the inverse of deformation rate). In contrast, Golecki et al.,[18] directly plotted centrifugal spinning RPM against viscosity values. However, our experimental results that show spinnability is quite different even if shear viscosity, relaxation time, and RPM are nearly matched, implying that both approaches are not suitable for evaluating spinnability as a function of solvent choice. Previously, Ren et al.[13] discussed the correlation between the diameter of centrifugally-spun fibers and this ratio, they called an elasticity processability

number ($P_e = \lambda_s/t_{evap}$). However, Ren et al.[13] did not contrast these two intrinsic timescales to determine spinnability. Even though Golecki et al.[18] discussed the role of evaporation, in their framework, matched viscosity and RPM lead to similar spinnability, in striking contrast with our observations. The "operating diagram" suggested by Fang *et al.* for reactive CFS,[15] contrasts the timescale for UV-induced polymerization and the extensional relaxation time, $\lambda_E$ along with time-of-flight. However, Fang et al. [15] relied on adding a large molecular weight PEO to dramatically enhance $\lambda_E$. In contrast, Table 1 shows all solutions used here for a fixed PEO concentration have comparable values of $\lambda_E$ that are proportional, but slightly lower in magnitude, compared with the corresponding values of $\lambda_s$. However, the evaporation time appears to have a twelve-fold variation and hence appears to induce the observed large variation in spinnability as a function of solvent composition.

Here we postulate that to the first order, the intrinsic differences in the rheology and evaporation of these entangled polymer solutions can be characterized in terms of the measured shear relaxation time, $\lambda_s$ (see Figure 3d) and the evaporation timescale determined from TGA measurements, $t_{evTGA}$ (Figure 5b) and listed in Table 1. In Figure 6a, we plot the values of $\lambda_s$ against $1/t_{evTGA}$ and we find that the continuous fibers appear above a critical value of the ratio of two timescale, which we call an intrinsic spinnability Deborah number, $De_s = \lambda_s/t_{evTGA}$. Here we assume that the timescale over which the liquid jet develops an elastic shell in centrifugal spinning would show a similar trend as observed for $t_{evTGA}$. To obtain a pragmatic and minimalistic description, we proceed without computing the conversion factor, expected to be a function of the processing conditions and macromolecular response. Hence, $De_s$=0.006, shown as a dotted line, marks the boundary between different regimes. As the sample placed in a TGA pan has a film thickness ~ 0.4 mm, just a tenfold decrease in thickness could shift this $De_s$ value by a hundredfold or more. Figure 6a shows that comparison of these two intrinsic timescales allows the creation of an intrinsic spinnability map, such that the transitions between

beaded fibers and no fibers, and between beaded and continuous fibers are demarcated by lines corresponding to constant $De_s$ values. Such a spinnability map has not been discussed before, and the captures observations for our experiments as the molecular weight, as well as processing conditions, including centrifugation speed, ambient conditions (temperature and humidity), nozzle to distance diameter, and nozzle size and properties, are left unchanged.

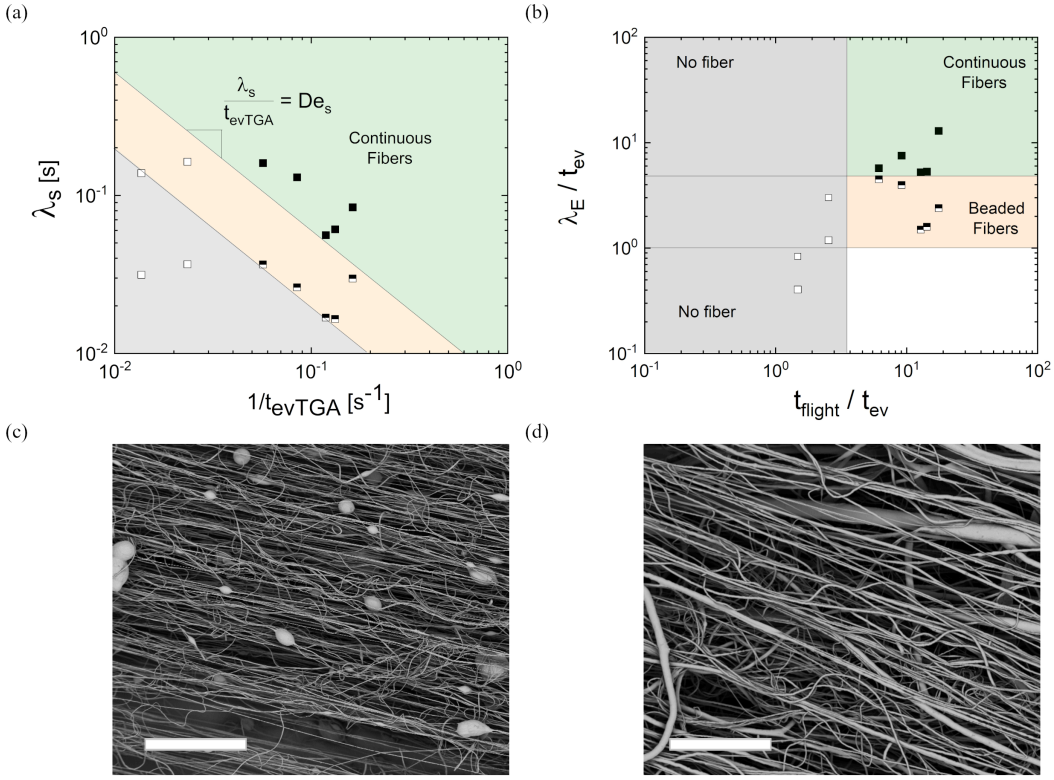


**Figure 6: Intrinsic spinnability diagram and a processability map.** (a) Shear relaxation time plotted against evaporation rate using the as-measured values obtained from the analysis of steady shear viscosity and mass loss via evaporation in TGA shows distinct regions of spinnable solutions above a certain $De_s$ values. (b) Comparison of three intrinsic timescales that capture the difference in evaporation time, relaxation time associated with viscoelasticity of the spinning drop, and time-of-flight set by processing conditions. Here a processability map emerges with regions of continuous fibers self-selecting a quadrant with slower relaxation and faster evaporation. Open symbols: no fibers, half-filled: (c) beaded fiber mats and closed symbols: continuous fibers, as shown in (d). The scale bar is 100 microns.

However, after a careful examination of physicochemical processes underlying spinnability, we infer that it would be helpful to supplement the intrinsic spinnability map based on shear rheological and mass loss timescales measured with standard techniques, with a

processability map, that explicitly accounts for the influence of time-of-flight that can be varied simply by changing spinning speed or nozzle-collector distance and accounts for extensional rheology response. We seek to draw a processability map that incorporates the influence of evaporation (solvent properties or ambient conditions), time-of-flight (RPM and nozzle-collector distance) and viscoelastic free surface flows (influenced by capillarity, elasticity, shear viscosity, and extensional rheology response). In Figure 6b, we present such a processability map sensitive to changes in the polymer ($M_w$, MWD, flexibility (determined by Kuhn segment size and number), and extensibility (ratio of fully-stretched chain length to coil size) and spinning conditions. The y-axis seeks to capture the influence of viscoelastic free surface flows and instabilities, whereas the x-axis aims to capture the influence of processing conditions like RPM and nozzle-collector distance. Here, we pick extensional relaxation time determined using capillarity-driven flows as the relevant measure, and as the processing conditions and polymer type are matched, we make a pragmatic estimate for evaporation time based on the value measured using TGA but scaled down by assuming 60 times smaller thickness than used in the TGA experiments. Here the choice of ratios of timescales is qualitatively inspired by the operating diagram from Fang et al.[15] The y-axis includes an extensional Deborah number, $De_E = \lambda_E/t_{ev}$ defined as the ratio of the extensional relaxation time to an evaporation time, $t_{ev}$. The x-axis choice contrasts the $t_{ev}$ and time-of-flight, $t_{flight}$.

Figure 6b, together with Table 1, suggests that the distinction between beads, beaded fibers (Figure 6c), and continuous fibers (see Figure 6d) here arise primarily due to the significant difference in the evaporation rate, for the relaxation time values change only by a factor of two, whereas evaporation rate changes by over twelve times. A closer look at viscosity and relaxation times for aqueous solutions shows that centrifugal spinning under matched conditions does provide a jet that neither dries nor breaks into drops before reaching the collector. Increasing the distance between nozzle and collector increases time-of-flight,

allowing centrifugal spinning from aqueous PEO solutions.[10] The diameter of 5 wt.% PEO solutions is greater than 3 wt.% solutions for matched solvent composition, and the change in morphology from the mat with few beads to continuous fibers at each solvent composition (shown in Figure 2) match quite well with the regimes identified in the processability map chartered in Figure 6b.

We recognize that in centrifugal spinning (and likewise for electrospinning), solvent evaporation is influenced by the flow field within the liquid jet and the complex airflow at the jet surface. The mass loss occurs from a cylindrical filament that decreases in diameter over time, and for some cases occurs from a cylinder that develops sinusoidal perturbations with associated variation in local evaporation rate. Additionally, we anticipate that the evaporation rate might be influenced by conformational changes of the polymers in response to extensional flows that arise in a jet that is drawn and stretched, and necks formed between growing beads. Thus, a rigorous and refined computation of $t_{ev}$ will require careful accounting of the following: (a) mass transfer coefficient under fiber spinning conditions, that accounts for changes in jet diameter, (b) the influence of polymer conformation and concentration while the jet travels from nozzle to collector, and (c) the role of convection currents within and around the spiraling jet, and interfacial flows and instabilities, among others. Likewise, we recognize that the shear relaxation time, $\lambda_s$ only quantifies the dynamics and rheology of mildly perturbed chains. We envision that $\lambda_E$ would capture the influence of polymer concentration or type, though we recognize that the deformation history, transients, and deformation rates encountered during fiber spinning need not be encountered or captured in most rheological measurements. Therefore, we reason that the strong correlation between the measured $\lambda_s$ and $\lambda_E$ (see Figure 4d) allows the construction of an intrinsic spinnability map shown in Figure 6a. An accurate and thorough assessment of the influence of change in polymer conformations and flow field within jets and around them on the timescales associated with instability growth, mass loss, and

overall time-of-flight is beyond the scope of present work. We speculate that such progress would require benefit from CFS experiments with in-situ analysis of concentration variation and flow fields, supplemented by computational fluid dynamics, with built-in nonlinear rheological and transport models.

The timescale for the growth of surface-tension-driven instabilities that lead to the formation of beaded fibers (see Figure 6c) or drop formation, and the formation of sinusoidal beads as well as the late-stage evolution of fiber diameter are influenced by an interplay of capillarity and viscoelasticity.[9, 102-106, 128, 129] Studies of jetting of viscoelastic fluids show that even though linear stability analysis predicts faster breakup than expected for Newtonian fluids of same viscosity, the pre-shear or unrelaxed tension delays the onset of sinusoidal perturbations.[101, 130-132] However, the drawing of jets and the late-stage pinching of necks or ligaments between beads are both influenced by extensional rheology response.[101-104, 128, 133] We infer that for volatile entangled (VE) polymer solutions, higher viscosity and unrelaxed tension contribute to a delayed appearance of sinusoidal perturbations, and rapid increase in viscosity on evaporation of volatile solvent stabilizes the jet. Furthermore, it appears that the prominent influence of initial instability growth on fiber morphology underlies the success of operating diagrams drawn using linear viscoelastic measures (like zero shear viscosity or shear relaxation time) and to the paradigm that entanglements facilitate electrospinnability.[87-89, 134, 135] We posit that the strong strain-hardening response and high Trouton ratios due to high extensibility of high molecular weight, flexible polymers (like PEO) in unentangled solutions can substantially delay pinching of necks and increase stringiness. The ultrahigh molecular weight, relatively high extensibility polymers can thus display extensibility-enriched (EE) spinnability in absence of entanglements, and many published examples show extensibility-enrichment provides pathway to make polysaccharide fibers,[136-140] and also fibers from unentangled solutions.[30, 135, 141] The choice of the ordinate in Figure 6b presents a straightforward corroboration of such

extensibility-enrichment in spinnability. We also infer that if the time-of-flight is long enough, a comparison of measured (or estimated) relaxation time and evaporation time facilitates distinction between the spinnable and non-spinnable solutions.

## CONCLUSIONS

This contribution shows that PEO fibers can be centrifugally spun using volatile, entangled (VE) solutions formulated using acetonitrile-water mixtures. We find that changing solvent properties by increasing AcN fraction influences spinnability and fiber morphology, using experiments carried out with a home-built CFS set-up for matched rotational speed (4000 rpm), room temperature and humidity, nozzle type/size/material, and distance to the collector. We find that the intrinsic spinnability map can be outlined using two measured timescales: the shear relaxation time, determined using steady shear viscosity measured using torsional rheometry and evaporation time, computed from the mass loss data acquired using thermogravimetric analysis (TGA). We anticipate that the intrinsic spinnability map is most suitable for the case described in this study that includes matched molecular weight and processing conditions, and nearly comparable shear viscosity and shear and extensional relaxation times despite variation in AcN fraction (or solvent composition). For fixed polymer concentration, only evaporation rates show an order of magnitude variation that provide the benchmark for determining spinnable cases. To provide a more generalized, but pragmatic portrait of spinnability, we draw a processability map that incorporates the influence of evaporation (solvent properties or ambient conditions), time-of-flight (RPM and nozzle-collector distance) and viscoelastic free surface flows (influenced by capillarity, elasticity, shear viscosity, and extensional rheology response) to identify spinnable formulations, and distinguish between different beads, beaded fiber and continuous fiber morphologies. In the processability map, we populate the y-axis with ratio of extensional relaxation time to evaporation time, and the x-axis with the ratio of time-of-flight to evaporation time. We

determined the extensional relaxation time using dripping-onto-substrate (DoS) rheometry to capture the likely influence of extensional rheology, stretched chain hydrodynamics and viscoelastic free surface flows and instabilities. We make a pragmatic estimate for evaporation time based on the value measured using TGA. We anticipate that despite its apparent simplicity, the processability map contains information comparable to a more rigorous portrait that accounts influence of change in polymer concentration and conformation during spinning on evaporation, instability growth and evolution, and chain relaxation timescales. Lastly, we postulate that a processability map that incorporates the influence of extensional relaxation time, evaporation time and processing time (time-of flight) can be utilized for designing and controlling volatile entangled (VE) and extensibility-enriched (EE) spinnability, and macromolecular engineering of spinnable formulations.

**ACKNOWLEDGEMENTS**

The authors (JM and NR) acknowledge IMO-IMOMEC at the University of Hasselt for providing financial support. CM would like to acknowledge funding support by the PPG Industries, CS Teaching Assistantship in the Department of Chemical Engineering at UIC, and VS the funds from 3M nontenured faculty award (NFTA). The U. Hasselt's Packaging Technology Center is acknowledged for providing access to the tensile testing machine and Dr. Jan D'Haen for access to the SEM. We acknowledge discussions with students from ODES-lab students at UIC. We thank Dr. Ruth Cardinaels (Leuven, Belgium) and Dr. Samanvaya Srivasatava (UCLA) for the close reading of an early draft. VS wishes to acknowledge the faculty, students, and staff in Textile Technology and CPSE, Indian Institute of Technology, Delhi, for training him as an undergraduate in various aspects of manufactured fiber technology and polymer science that have contributed to the ideas in this paper (twenty years later!).

## REFERENCES


1. Atıcı, B.; Ünlü, C. H.; Yanilmaz, M. A review on centrifugally spun fibers and their applications. *Polymer Reviews* **2021**, 1-64.
2. Dos Santos, D. M.; Correa, D. S.; Medeiros, E. S.; Oliveira, J. E.; Mattoso, L. H. Advances in functional polymer nanofibers: From spinning fabrication techniques to recent biomedical applications. *ACS Applied Materials & Interfaces* **2020,** 12 (41), 45673-45701.
3. Zhang, X.; Lu, Y. Centrifugal spinning: an alternative approach to fabricate nanofibers at high speed and low cost. *Polymer Reviews* **2014,** 54 (4), 677-701.
4. Sarkar, K.; Gomez, C.; Zambrano, S.; Ramirez, M.; de Hoyos, E.; Vasquez, H.; Lozano, K. Electrospinning to forcespinning™. *Mater. Today* **2010,** 13 (11), 12-14.
5. Badrossamay, M. R.; McIlwee, H. A.; Goss, J. A.; Parker, K. K. Nanofiber assembly by rotary jet-spinning. *Nano Lett.* **2010,** 10 (6), 2257-2261.
6. Rogalski, J. J.; Bastiaansen, C. W.; Peijs, T. Rotary jet spinning review–a potential high yield future for polymer nanofibers. *Nanocomposites* **2017,** 3 (4), 97-121.
7. Kwak, B. E.; Yoo, H. J.; Lee, E.; Kim, D. H. Large-Scale Centrifugal Multispinning Production of Polymer Micro-and Nanofibers for Mask Filter Application with a Potential of Cospinning Mixed Multicomponent Fibers. *ACS Macro Lett.* **2021,** 10 (3), 382-388.
8. Stojanovska, E.; Canbay, E.; Pampal, E. S.; Calisir, M. D.; Agma, O.; Polat, Y.; Simsek, R.; Gundogdu, N. S.; Akgul, Y.; Kilic, A. A review on non-electro nanofibre spinning techniques. *RSC Advances* **2016,** 6 (87), 83783-83801.
9. Park, J. H.; Rutledge, G. C. 50th anniversary perspective: advanced polymer fibers: high performance and ultrafine. *Macromolecules* **2017,** 50 (15), 5627-5642.
10. Noroozi, S.; Arne, W.; Larson, R. G.; Taghavi, S. M. A comprehensive mathematical model for nanofibre formation in centrifugal spinning methods. *J. Fluid Mech.* **2020,** 892.
11. Taghavi, S. M.; Larson, R. G. Regularized thin-fiber model for nanofiber formation by centrifugal spinning. *Phys. Rev. E.* **2014,** 89 (2), 023011.
12. Divvela, M. J.; Ruo, A.-C.; Zhmayev, Y.; Joo, Y. L. Discretized modeling for centrifugal spinning of viscoelastic liquids. *J. Non-Newtonian Fluid Mech.* **2017,** 247, 62-77.
13. Ren, L.; Ozisik, R.; Kotha, S. P.; Underhill, P. T. Highly efficient fabrication of polymer nanofiber assembly by centrifugal jet spinning: process and characterization. *Macromolecules* **2015,** 48 (8), 2593-2602.
14. Noroozi, S.; Alamdari, H.; Arne, W.; Larson, R. G.; Taghavi, S. M. Regularized string model for nanofibre formation in centrifugal spinning methods. *J. Fluid Mech.* **2017,** 822, 202-234.
15. Fang, Y.; Dulaney, A. D.; Gadley, J.; Maia, J. M.; Ellison, C. J. Manipulating characteristic timescales and fiber morphology in simultaneous centrifugal spinning and photopolymerization. *Polymer* **2015,** 73, 42-51.
16. Fang, Y.; Dulaney, A. R.; Gadley, J.; Maia, J.; Ellison, C. J. A comparative parameter study: Controlling fiber diameter and diameter distribution in centrifugal spinning of photocurable monomers. *Polymer* **2016,** 88, 102-111.
17. Merchiers, J.; Meurs, W.; Deferme, W.; Peeters, R.; Buntinx, M.; Reddy, N. K. Influence of polymer concentration and nozzle material on centrifugal fiber spinning. *Polymers* **2020,** 12 (3), 575.
18. Golecki, H. M.; Yuan, H.; Glavin, C.; Potter, B.; Badrossamay, M. R.; Goss, J. A.; Phillips, M. D.; Parker, K. K. Effect of solvent evaporation on fiber morphology in rotary jet spinning. *Langmuir* **2014,** 30 (44), 13369-13374.
19. Veleirinho, B.; Rei, M. F.; Lopes ‐ D.A ‐ Silva, J. A. Solvent and concentration effects on the properties of electrospun poly (ethylene terephthalate) nanofiber mats. *J. Polym. Sci., Part B: Polym. Phys.* **2008,** 46 (5), 460-471.

20. Hou, T.; Li, X.; Lu, Y.; Yang, B. Highly porous fibers prepared by centrifugal spinning. *Materials & Design* **2017,** 114, 303-311.
21. Son, W. K.; Youk, J. H.; Lee, T. S.; Park, W. H. The effects of solution properties and polyelectrolyte on electrospinning of ultrafine poly (ethylene oxide) fibers. *polymer* **2004,** 45 (9), 2959-2966.
22. Fong, H.; Chun, I.; Reneker, D. H. Beaded nanofibers formed during electrospinning. *Polymer* **1999,** 40 (16), 4585-4592.
23. Tripatanasuwan, S.; Zhong, Z.; Reneker, D. H. Effect of evaporation and solidification of the charged jet in electrospinning of poly (ethylene oxide) aqueous solution. *Polymer* **2007,** 48 (19), 5742-5746.
24. Pham, Q. P.; Sharma, U.; Mikos, A. G. Electrospinning of polymeric nanofibers for tissue engineering applications: a review. *Tissue Eng.* **2006,** 12 (5), 1197-1211.
25. Ding, B.; Yu, J., *Electrospun nanofibers for energy and environmental applications*. Springer: 2014.
26. Padron, S.; Patlan, R.; Gutierrez, J.; Santos, N.; Eubanks, T.; Lozano, K. Production and characterization of hybrid BEH‐PPV/PEO conjugated polymer nanofibers by forcespinning™. *J. Appl. Polym. Sci.* **2012,** 125 (5), 3610-3616.
27. Mahalingam, S.; Edirisinghe, M. Forming of polymer nanofibers by a pressurised gyration process. *Macromol. Rapid Commun.* **2013,** 34 (14), 1134-1139.
28. Jaeger, R.; Bergshoef, M. M.; Batlle, C. M. I.; Schönherr, H.; Julius Vancso, G. In *Electrospinning of ultra‐thin polymer fibers*, Macromolecular symposia, 1998; Wiley Online Library: 1998; pp 141-150.
29. Doshi, J.; Reneker, D. H. Electrospinning process and applications of electrospun fibers. *Journal of Electrostatics* **1995,** 35 (2-3), 151-160.
30. Yu, J. H.; Fridrikh, S. V.; Rutledge, G. C. The role of elasticity in the formation of electrospun fibers. *Polymer* **2006,** 47 (13), 4789-4797.
31. Helgeson, M. E.; Grammatikos, K. N.; Deitzel, J. M.; Wagner, N. J. Theory and kinematic measurements of the mechanics of stable electrospun polymer jets. *Polymer* **2008,** 49 (12), 2924-2936.
32. Richard-Lacroix, M.; Pellerin, C. Molecular orientation in electrospun fibers: from mats to single fibers. *Macromolecules* **2013,** 46 (24), 9473-9493.
33. Barhoum, A.; Pal, K.; Rahier, H.; Uludag, H.; Kim, I. S.; Bechelany, M. Nanofibers as new-generation materials: from spinning and nano-spinning fabrication techniques to emerging applications. *Applied Materials Today* **2019,** 17, 1-35.
34. Bianco, A.; Calderone, M.; Cacciotti, I. Electrospun PHBV/PEO co-solution blends: Microstructure, thermal and mechanical properties. *Materials Science and Engineering: C* **2013,** 33 (3), 1067-1077.
35. Chavez, R. O.; Lodge, T. P.; Alcoutlabi, M. Recent developments in centrifugally spun composite fibers and their performance as anode materials for lithium-ion and sodium-ion batteries. *Materials Science and Engineering: B* **2021,** 266, 115024.
36. Hasan, M. T.; Gonzalez, R.; Chipara, M.; Materon, L.; Parsons, J.; Alcoutlabi, M. Antibacterial activities of centrifugally spun polyethylene oxide/silver composite nanofibers. *Polym. Adv. Technol.* **2021,** 32 (6), 2327-2338.
37. Sullivan, S. T.; Tang, C.; Kennedy, A.; Talwar, S.; Khan, S. A. Electrospinning and heat treatment of whey protein nanofibers. *Food Hydrocoll.* **2014,** 35, 36-50.
38. Venugopal, J.; Ramakrishna, S. Applications of polymer nanofibers in biomedicine and biotechnology. *Appl. Biochem. Biotechnol.* **2005,** 125 (3), 147-157.
39. Li, X.; Lu, Y.; Hou, T.; Zhou, J.; Yang, B. Centrifugally spun ultrafine starch/PEO fibres as release formulation for poorly water-soluble drugs. *Micro & Nano Letters* **2018,** 13 (12), 1688-1692.

40. Samad, Y. A.; Asghar, A.; Hashaikeh, R. Electrospun cellulose/PEO fiber mats as a solid polymer electrolytes for Li ion batteries. *Renewable Energy* **2013,** 56, 90-95.
41. Dinic, J.; Zhang, Y.; Jimenez, L. N.; Sharma, V. Extensional relaxation times of dilute, aqueous polymer solutions. *ACS Macro Lett.* **2015,** 4 (7), 804-808.
42. Dinic, J.; Biagioli, M.; Sharma, V. Pinch‐off dynamics and extensional relaxation times of intrinsically semi‐dilute polymer solutions characterized by dripping‐onto‐substrate rheometry. *J. Polym. Sci., Part B: Polym. Phys.* **2017,** 55 (22), 1692-1704.
43. Dinic, J.; Sharma, V. Macromolecular relaxation, strain, and extensibility determine elastocapillary thinning and extensional viscosity of polymer solutions. *Proc. Natl. Acad. Sci. U.S.A.* **2019,** 116 (18), 8766–8774.
44. Dinic, J.; Sharma, V. Flexibility, extensibility, and ratio of Kuhn length to packing length govern the pinching gynamics, coil-stretch transition, and rheology of polymer solutions. *Macromolecules* **2020,** 53, 4821-4835.
45. Martínez Narváez, C. D. V.; Mazur, T.; Sharma, V. Dynamics and extensional rheology of polymer-surfactant association complexes. *Soft Matter* **2021,** 17, 6116-6126.
46. Merchiers, J.; Martínez Narváez, C. D. V.; Slykas, C.; Buntinx, M.; Deferme, W.; D'Haen, J.; Peeters, R.; Sharma, V.; Reddy, N. K. Centrifugally spun PEO fibers rival the properties of electrospun fibers. *J. Polym. Sci.* **2021**, DOI: 10.1002/pol.20210424.
47. Clasen, C.; Phillips, P. M.; Palangetic, L. Dispensing of rheologically complex fluids: the map of misery. *AlChE J.* **2012,** 58 (10), 3242-3255.
48. Ziabicki, A., *Fundamentals of Fibre Formation*. John Wiley & Sons: New York, 1976.
49. Gupta, V. B.; Kothari, V. K., *Manufactured Fiber Technology*. Chapman & Hall: London, 1997.
50. Tripathi, A.; Whittingstall, P.; McKinley, G. H. Using filament stretching rheometry to predict strand formation and "processability" in adhesives and other non-Newtonian fluids. *Rheol. Acta* **2000,** 39 (4), 321-337.
51. Petrie, C. J. S. One hundred years of extensional flow. *J. Non-Newtonian Fluid Mech.* **2006,** 137 (1-3), 1-14 DOI: 10.1016/j.jnnfm.2006.01.010.
52. Larson, R. G. Spinnability and viscoelasticity. *J. Non-Newtonian Fluid Mech.* **1983,** 12 (3), 303-315.
53. Dinic, J.; Jimenez, L. N.; Sharma, V. Pinch-off dynamics and dripping-onto-substrate (DoS) rheometry of complex fluids. *Lab Chip* **2017,** 17, 460-473.
54. Dinic, J.; Sharma, V. Power laws dominate shear and extensional rheology response and capillarity-driven pinching dynamics of entangled hydrodyethyl cellulose (HEC) solutions. *Macromolecules* **2020,** 53, 3424-3437.
55. Jimenez, L. N.; Dinic, J.; Parsi, N.; Sharma, V. Extensional relaxation time, pinch-off dynamics and printability of semi-dilute polyelectrolyte solutions *Macromolecules* **2018,** 51 (14), 5191-5208.
56. Jimenez, L. N.; Martínez Narváez, C. D. V.; Sharma, V. Capillary breakup and extensional rheology response of food thickener cellulose gum (NaCMC) in salt-free and excess salt solutions. *Phys. Fluids* **2020,** 32, 012113.
57. Martínez Narváez, C. D.; Dinic, J.; Lu, X.; Wang, C.; Rock, R.; Sun, H.; Sharma, V. Rheology and pinching dynamics of associative polysaccharide solutions. *Macromolecules* **2021,** 54, 6372−6388.
58. Jimenez, L. N.; Narváez, C. D. M.; Xu, C.; Bacchi, S.; Sharma, V. The rheologically-complex fluid beauty of nail lacquer formulations. *Soft Matter* **2021,** in press.
59. Jimenez, L. N.; Narváez, C. D. V. M.; Xu, C.; Bacchi, S.; Sharma, V. Rheological properties influence tackiness, application and performance of nail polish/lacquer formulations. *Surface Science and Adhesion in Cosmetics* **2021**, 109-150.

60. Walter, A. V.; Jimenez, L. N.; Dinic, J.; Sharma, V.; Erk, K. A. Effect of salt valency and concentration on shear and extensional rheology of aqueous polyelectrolyte solutions for enhanced oil recovery. *Rheol. Acta* **2019,** 58, 145-157.
61. Hsiao, K. W.; Dinic, J.; Ren, Y.; Sharma, V.; Schroeder, C. M. Passive non-linear microrheology for determining extensional viscosity. *Phys. Fluids* **2017,** 29 (12), 121603 DOI: 10.1063/1.4993736.
62. Marshall, K. A.; Liedtke, A. M.; Todt, A. H.; Walker, T. W. Extensional rheometry with a handheld mobile device. *Exp. Fluids* **2017,** 58:69, 9 DOI: 10.1007/s00348-017-2351-9.
63. Marshall, K. A.; Walker, T. W. Investigating the dynamics of droplet breakup in a microfluidic cross-slot device for characterizing the extensional properties of weakly-viscoelastic fluids. *Rheol. Acta* **2019,** 58 (9), 573-590.
64. Rosello, M.; Sur, S.; Barbet, B.; Rothstein, J. P. Dripping-onto-substrate capillary breakup extensional rheometry of low-viscosity printing inks. *J. Non-Newtonian Fluid Mech.* **2019,** 266, 160-170.
65. Pack, M. Y.; Yang, A.; Perazzo, A.; Qin, B.; Stone, H. A. Role of extensional rheology on droplet bouncing. *Phys. Rev. Fluids* **2019,** 4 (12), 123603.
66. Su, Y.; Palacios, B.; Zenit, R. Coiling of a viscoelastic fluid filament. *Phys. Rev. Fluids* **2021,** 6 (3), 033303.
67. Murdoch, T. J.; Pashkovski, E.; Patterson, R.; Carpick, R. W.; Lee, D. Sticky but Slick: Reducing Friction Using Associative and Nonassociative Polymer Lubricant Additives. *ACS Applied Polymer Materials* **2020,** 2 (9), 4062-4070.
68. Wu, S.; Mohammadigoushki, H. Linear versus branched: flow of a wormlike micellar fluid past a falling sphere. *Soft Matter* **2021,** 17 (16), 4395-4406.
69. Xu, M.; Li, X.; Riseman, A.; Frostad, J. M. Quantifying the effect of extensional rheology on the retention of agricultural sprays. *Phys. Fluids* **2021,** 33 (3), 032107.
70. Franco-Gómez, A.; Onuki, H.; Yokoyama, Y.; Nagatsu, Y.; Tagawa, Y. Effect of liquid elasticity on the behaviour of high-speed focused jets. *Exp. Fluids* **2021,** 62 (2), 1-15.
71. Jafari Nodoushan, E.; Lee, Y. J.; Lee, G.-H.; Kim, N. Quasi-static secondary flow regions formed by microfluidic contraction flows of wormlike micellar solutions. *Phys. Fluids* **2021,** 33 (9), 093112.
72. Clasen, C.; Plog, J. P.; Kulicke, W. M.; Owens, M.; Macosko, C.; Scriven, L. E.; Verani, M.; McKinley, G. H. How dilute are dilute solutions in extensional flows? *J. Rheol.* **2006,** 50 (6), 849-881 DOI: 10.1122/1.2357595.
73. Tirtaatmadja, V.; McKinley, G. H.; Cooper-White, J. J. Drop formation and breakup of low viscosity elastic fluids: Effects of molecular weight and concentration. *Phys. Fluids* **2006,** 18 (4), 043101.
74. Schroeder, C. M. Single polymer dynamics for molecular rheology. *J. Rheol.* **2018,** 62 (1), 371-403.
75. Somani, S.; Shaqfeh, E. S. G.; Prakash, J. R. Effect of solvent quality on the coil-stretch transition. *Macromolecules* **2010,** 43 (24), 10679-10691 DOI: 10.1021/ma1019945.
76. Sasmal, C.; Hsiao, K.-W.; Schroeder, C. M.; Ravi Prakash, J. Parameter-free prediction of DNA dynamics in planar extensional flow of semidilute solutions. *J. Rheol.* **2017,** 61 (1), 169-186.
77. Hsiao, K.-W.; Sasmal, C.; Ravi Prakash, J.; Schroeder, C. M. Direct observation of DNA dynamics in semidilute solutions in extensional flow. *J. Rheol.* **2017,** 61 (1), 151-167.
78. Prabhakar, R.; Prakash, J. R.; Sridhar, T. Effect of configuration-dependent intramolecular hydrodynamic interaction on elastocapillary thinning and breakup of filaments of dilute polymer solutions. *Journal of Rheology* **2006,** 50 (6), 925-947.

79. Prabhakar, R.; Gadkari, S.; Gopesh, T.; Shaw, M. J. Influence of stretching induced self-concentration and self-dilution on coil-stretch hysteresis and capillary thinning of unentangled polymer solutions. *J. Rheol.* **2016,** 60 (3), 345-366.
80. Prabhakar, R.; Sasmal, C.; Nguyen, D. A.; Sridhar, T.; Prakash, J. R. Effect of stretching-induced changes in hydrodynamic screening on coil-stretch hysteresis of unentangled polymer solutions. *Phys. Rev. Fluids* **2017,** 2 (1), 011301.
81. Prakash, J. R. Universal dynamics of dilute and semidilute solutions of flexible linear polymers. *Curr. Opin. Colloid Interface Sci.* **2019,** 43, 63-79.
82. Matsumiya, Y.; Watanabe, H. Non-Universal features in uniaxially extensional rheology of linear polymer melts and concentrated solutions: A review. *Prog. Polym. Sci.* **2020**, 101325.
83. Desai, P. S.; Larson, R. G. Constitutive model that shows extension thickening for entangled solutions and extension thinning for melts. *J. Rheol.* **2014,** 58 (1), 255-279.
84. Bird, R. B.; Armstrong, R. C.; Hassager, O., *Dynamics of Polymeric Liquids*. 2nd ed.; John Wiley & Sons: New York, 1987; Vol. 1.
85. Rubinstein, M.; Colby, R. H., *Polymer Physics*. Oxford Univ. Press: New York: 2003.
86. Shankar, R.; Klossner, R. R.; Weaver, J. T.; Koga, T.; van Zanten, J. H.; Krause, W. E.; Colina, C. M.; Tanaka, F.; Spontak, R. J. Competitive hydrogen-bonding in polymer solutions with mixed solvents. *Soft Matter* **2009,** 5 (2), 304-307.
87. Shenoy, S. L.; Bates, W. D.; Frisch, H. L.; Wnek, G. E. Role of chain entanglements on fiber formation during electrospinning of polymer solutions: good solvent, non-specific polymer–polymer interaction limit. *Polymer* **2005,** 46 (10), 3372-3384.
88. Gupta, P.; Elkins, C.; Long, T. E.; Wilkes, G. L. Electrospinning of linear homopolymers of poly (methyl methacrylate): exploring relationships between fiber formation, viscosity, molecular weight and concentration in a good solvent. *Polymer* **2005,** 46 (13), 4799-4810.
89. Haward, S. J.; Sharma, V.; Butts, C. P.; McKinley, G. H.; Rahatekar, S. S. Shear and extensional rheology of cellulose/ionic liquid solutions. *Biomacromolecules* **2012,** 13 (5), 1688-1699.
90. McKinley, G. H. Visco-elasto-capillary thinning and break-up of complex fluids. *Rheology Reviews* **2005**, 1-48.
91. Bazilevsky, A. V.; Entov, V. M.; Rozhkov, A. N. In *Liquid filament microrheometer and some of its applications*, Third European Rheology Conference and Golden Jubilee Meeting of the British Society of Rheology, Edinburgh, UK, 1990; Elsevier: Edinburgh, UK, 1990; pp 41-43.
92. Bazilevsky, A. V.; Entov, V. M.; Rozhkov, A. N. Breakup of a liquid bridge as a method of rheological testing of biological fluids. *Fluid Dynamics* **2011,** 46 (4), 613-622.
93. Rodd, L. E.; Scott, T. P.; Cooper-White, J. J.; McKinley, G. H. Capillary break-up rheometry of low-viscosity elastic fluids. *Appl. Rheol.* **2005,** 15 (1), 12-27.
94. Arnolds, O.; Buggisch, H.; Sachsenheimer, D.; Willenbacher, N. Capillary breakup extensional rheometry (CaBER) on semi-dilute and concentrated polyethyleneoxide (PEO) solutions. *Rheol. Acta* **2010,** 49 (11-12), 1207-1217.
95. Vadillo, D. C.; Mathues, W.; Clasen, C. Microsecond relaxation processes in shear and extensional flows of weakly elastic polymer solutions. *Rheol. Acta* **2012,** 51 (8), 755-769.
96. Anna, S. L.; McKinley, G. H. Elasto-capillary thinning and breakup of model elastic liquids. *J. Rheol.* **2001,** 45 (1), 115-138.
97. Campo-Deano, L.; Clasen, C. The slow retraction method (SRM) for the determination of ultra-short relaxation times in capillary breakup extensional rheometry experiments. *J. Non-Newtonian Fluid Mech.* **2010,** 165 (23), 1688-1699.

98. Morozova, S.; Schmidt, P. W.; Metaxas, A.; Bates, F. S.; Lodge, T. P.; Dutcher, C. S. Extensional flow behavior of methylcellulose solutions containing fibrils. *ACS MacroLetters* **2018,** 7 (3), 347-352 DOI: 10.1021/acsmacrolett.8b00042.
99. Wagner, C.; Amarouchene, Y.; Bonn, D.; Eggers, J. Droplet detachment and satellite bead formation in viscoelastic fluids. *Phys. Rev. Lett.* **2005,** 95 (16), DOI: 164504 10.1103/PhysRevLett.95.164504.
100. Sattler, R.; Gier, S.; Eggers, J.; Wagner, C. The final stages of capillary break-up of polymer solutions. *Phys. Fluids* **2012,** 24 (2), 023101.
101. Yarin, A. L., *Free Liquid Jets and Films: Hydrodynamics and Rheology*. Longman Scientific & Technical: 1993.
102. Sharma, V.; Haward, S. J.; Serdy, J.; Keshavarz, B.; Soderlund, A.; Threlfall-Holmes, P.; McKinley, G. H. The rheology of aqueous solutions of Ethyl Hydroxy-Ethyl Cellulose (EHEC) and its hydrophobically modified Analogue (hmEHEC): Extensional flow response in capillary break-up, jetting (ROJER) and in a cross-slot extensional rheometer. *Soft Matter* **2015,** 11 (16), 3251-3270.
103. Sharma, V.; Ardekani, A. M.; McKinley, G. H. 'Beads on a string' structures and extensional rheometry using jet break-up. *5th Pacific Rim Conference on Rheology (PRCR-5)* **2010**.
104. Ardekani, A.; Sharma, V.; McKinley, G. H. Dynamics of bead formation, filament thinning and breakup of weakly viscoelastic jets. *J. Fluid Mech.* **2010,** 665, 46-56.
105. Greiciunas, E.; Wong, J.; Gorbatenko, I.; Hall, J.; Wilson, M. C. T.; Kapur, N.; Harlen, O. G.; Vadillo, D.; Threlfall-Holmes, P. Design and operation of a Rayleigh Ohnesorge jetting extensional rheometer (ROJER) to study extensional properties of low viscosity polymer solutions. *J. Rheol.* **2017,** 61 (3), 467-476 DOI: 10.1122/1.4979099.
106. Mathues, W.; Formenti, S.; McIlroy, C.; Harlen, O. G.; Clasen, C. CaBER vs ROJER-Different time scales for the thinning of a weakly elastic jet. *J. Rheol.* **2018,** 62 (5), 1135-1153 DOI: 10.1122/1.5021834.
107. Entov, V. M.; Hinch, E. J. Effect of a spectrum of relaxation times on the capillary thinning of a filament of elastic liquid. *J. Non-Newtonian Fluid Mech.* **1997,** 72, 31-54.
108. Zhou, J.; Doi, M. Dynamics of viscoelastic filaments based on Onsager principle. *Phys. Rev. Fluids* **2018,** 3 (8), 084004.
109. Wagner, C.; Bourouiba, L.; McKinley, G. H. An analytic solution for capillary thinning and breakup of FENE-P fluids. *J. Non-Newtonian Fluid Mech.* **2015,** 218, 53-61.
110. Eggers, J.; Herrada, M. A.; Snoeijer, J. H. Self-similar breakup of polymeric threads as described by the Oldroyd-B model. *J. Fluid Mech.* **2020,** 887.
111. Deblais, A.; Herrada, M. A.; Eggers, J.; Bonn, D. Self-similarity in the breakup of very dilute viscoelastic solutions. *J. Fluid Mech.* **2020,** 904.
112. Bhat, P. P.; Appathurai, S.; Harris, M. T.; Pasquali, M.; McKinley, G. H.; Basaran, O. A. Formation of beads-on-a-string structures during break-up of viscoelastic filaments. *Nature Physics* **2010,** 6 (8), 625-631.
113. Larson, R. G., *Constitutive Equations for Polymer Solutions and Melts*. Butterworth Publishers: Boston, 1988.
114. Yaoita, T.; Isaki, T.; Masubuchi, Y.; Watanabe, H.; Ianniruberto, G.; Marrucci, G. Primitive chain network simulation of elongational flows of entangled linear chains: Role of finite chain extensibility. *Macromolecules* **2011,** 44 (24), 9675–9682.
115. Yaoita, T.; Isaki, T.; Masubuchi, Y.; Watanabe, H.; Ianniruberto, G.; Marrucci, G. Primitive Chain Network Simulation of Elongational Flows of Entangled Linear Chains: Stretch/Orientation-induced Reduction of Monomeric Friction. *Macromolecules* **2012,** 45 (6), 2773-2782 DOI: 10.1021/ma202525v.

116. Bobbili, S. V.; Milner, S. T. Chain tension reduces monomer friction in simulated polymer melts. *J. Rheol.* **2020,** 64 (6), 1373-1378.
117. Kushwaha, A.; Shaqfeh, E. S. G. Slip-link simulations of entangled polymers in planar extensional flow: Disentanglement modified extensional thinning. *J. Rheol.* **2011,** 55 (3), 463-483 DOI: 10.1122/1.3549296.
118. Ye, X.; Larson, R. G.; Pattamaprom, C.; Sridhar, T. Extensional properties of monodisperse and bidisperse polystyrene solutions. *J. Rheol.* **2003,** 47 (2), 443-468 DOI: 10.1122/1.1545079.
119. Rasmussen, H. K.; Wingstrand, S. L.; Hassager, O. On the universality in the extensional rheology of monodisperse polymer melts and oligomer dilutions thereof. *Rheol. Acta* **2019,** 58 (6), 333-340.
120. Huang, Q.; Hengeller, L.; Alvarez, N. J.; Hassager, O. Bridging the gap between polymer melts and solutions in extensional rheology. *Macromolecules* **2015,** 48 (12), 4158-4163.
121. Huang, Q.; Mednova, O.; Rasmussen, H. K.; Alvarez, N. J.; Skov, A. L.; Almdal, K.; Hassager, O. Concentrated polymer solutions are different from melts: Role of entanglement molecular weight. *Macromolecules* **2013,** 46 (12), 5026-5035.
122. Suteria, N. S.; Gupta, S.; Potineni, R.; Baier, S. K.; Vanapalli, S. A. eCapillary: a disposable microfluidic extensional viscometer for weakly elastic polymeric fluids. *Rheol. Acta* **2019,** 58, 403-417.
123. Larson, R. G. The rheology of dilute solutions of flexible polymers: Progress and problems. *J. Rheol.* **2005,** 49 (1), 1-70 DOI: 10.1122/1.1835336.
124. McKinley, G. H.; Sridhar, T. Filament-stretching rheometry of complex fluids. *Ann. Rev. Fluid. Mech.* **2002,** 34, 375-415.
125. Sharma, V.; Song, L.; Jones, R. L.; Barrow, M. S.; Williams, P. R.; Srinivasarao, M. Effect of solvent choice on breath-figure-templated assembly of. *EPL (Europhysics Letters)* **2010,** 91 (3), 38001.
126. Crank, J., *The Mathematics of Diffusion*. 2nd ed.; Oxford University Press: 1979.
127. Eggers, J. Nonlinear dynamics and breakup of free-surface flows. *Rev. Mod. Phys.* **1997,** 69 (3), 865-929.
128. Clasen, C.; Eggers, J.; Fontelos, M. A.; Li, J.; McKinley, G. H. The beads-on-string structure of viscoelastic threads. *J. Fluid Mech.* **2006,** 556, 283-308 DOI: 10.1017/s0022112006009633.
129. Middleman, S. Stability of a viscoelastic jet. *Chem. Eng. Sci.* **1965,** 20 (12), 1037-1040.
130. Goldin, M.; Yerushalmi, J.; Pfeffer, R.; Shinnar, R. Breakup of a laminar capillary jet of a viscoelastic fluid. *J. Fluid Mech.* **1969,** 38 (4), 689-711.
131. Bazilevskii, A. V.; Entov, V. M.; Rozhkov, A. N. Elastic stresses in capillary jets of dilute polymer solutions. *Fluid Dynamics* **1985,** 20 (2), 169-175.
132. Mun, R. P.; Byars, J. A.; Boger, D. V. The effects of polymer concentration and molecular weight on the breakup of laminar capillary jets. *J. Non-Newtonian Fluid Mech.* **1998,** 74 (1-3), 285-297.
133. Bousfield, D. W.; Keunings, R.; Marrucci, G.; Denn, M. M. Nonlinear analysis of the surface tension driven breakup of viscoelastic filaments. *J. Non-Newtonian Fluid Mech.* **1986,** 21 (1), 79-97.
134. McKee, M. G.; Wilkes, G. L.; Colby, R. H.; Long, T. E. Correlations of solution rheology with electrospun fiber formation of linear and branched polyesters. *Macromolecules* **2004,** 37 (5), 1760-1767.
135. Palangetic, L.; Reddy, N. K.; Srinivasan, S.; Cohen, R. E.; McKinley, G. H.; Clasen, C. Dispersity and spinnability: Why highly polydisperse polymer solutions are desirable for electrospinning. *Polymer* **2014,** 55 (19), 4920-4931.

136. Rošic, R.; Pelipenko, J.; Kocbek, P.; Baumgartner, S.; Bešter-Rogač, M.; Kristl, J. The role of rheology of polymer solutions in predicting nanofiber formation by electrospinning. *Eur. Polym. J.* **2012,** 48 (8), 1374-1384.
137. Mengistu Lemma, S.; Bossard, F.; Rinaudo, M. Preparation of pure and stable chitosan nanofibers by electrospinning in the presence of poly (ethylene oxide). *International Journal of Molecular Sciences* **2016,** 17 (11), 1790.
138. Mirtič, J.; Balažic, H.; Zupančič, Š.; Kristl, J. Effect of solution composition variables on electrospun alginate nanofibers: Response surface analysis. *Polymers* **2019,** 11 (4), 692.
139. Rieger, K. A.; Birch, N. P.; Schiffman, J. D. Electrospinning chitosan/poly (ethylene oxide) solutions with essential oils: Correlating solution rheology to nanofiber formation. *Carbohydr. Polym.* **2016,** 139, 131-138.
140. Pakravan, M.; Heuzey, M.-C.; Ajji, A. A fundamental study of chitosan/PEO electrospinning. *Polymer* **2011,** 52 (21), 4813-4824.
141. Malkin, A. Y.; Semakov, A. V.; Skvortsov, I. Y.; Zatonskikh, P.; Kulichikhin, V. G.; Subbotin, A. V.; Semenov, A. N. Spinnability of dilute polymer solutions. *Macromolecules* **2017,** 50 (20), 8231-8244.